High Thermoelectric Power Factor in Intermetallic CoSi Arising from Energy Filtering of Electrons by Phonon Scattering

Yi Xia,[1,*] Junsoo Park,[2] Fei Zhou,[3] and Vidvuds Ozoliņš[4,5,†]

[1] *Department of Materials Science and Engineering, Northwestern University, Evanston, Illinois 60208, USA*

[2] *Department of Materials Science and Engineering, University of California, Los Angeles, California 90095, USA*

[3] *Physical and Life Sciences Directorate, Lawrence Livermore National Laboratory, Livermore, California 94550, USA*

[4] *Department of Applied Physics, Yale University, New Haven, Connecticut 06511, USA*

[5] *Energy Sciences Institute, Yale University, West Haven, Connecticut 06516, USA*

Intermetallic compounds are usually poor thermoelectrics due to the high electronic densities of states at the Fermi level and concomitantly low Seebeck coefficients. However, intermetallic $B20$-type CoSi has been experimentally shown to attain remarkably large negative values of the Seebeck coefficient. We provide a theoretical explanation for this surprising fact using state-of-the-art first-principles calculations with explicit treatment of electron-phonon interactions. We find that the unique band structure of CoSi, which has both massless and heavy fermion bands near the Fermi level, facilitates strong scattering of the low-energy electrons by phonons into the heavy band, resulting in effective energy filtering and high thermal voltage. Our study predicts that a very large thermoelectric power factor of 80 μW cm^{-1} K^{-2} or higher is experimentally accessible in the 300–600 K range and highlights a general principle for identifying intermetallic compounds with large thermopower.

I. INTRODUCTION

Promising advances have been made in the last decade toward increasing the efficiency of thermoelectric materials for their potential applications in waste-heat recovery and thermal cooling [1–5]. The thermoelectric efficiency is characterized by the figure of merit defined as $ZT = \sigma S^2 T/(\kappa_e + \kappa_l)$. Here, S is the Seebeck coefficient; σ is electrical conductivity; κ_e and κ_l are, respectively, thermal conductivities due to electrons and lattice vibrations; and σS^2 is referred to as the thermoelectric power factor (PF). The central challenge is the simultaneous optimization of these properties, since their changes in response to design parameters often have competing ("contraindicated") effects on ZT [1,2,6]. The relatively decoupled relation between the electronic conductivity and phonon-mediated heat transport has led to several major successes in improving ZT by reducing κ_l. Enhancement of the phonon scattering by utilizing strong intrinsic anharmonicity, nanostructures, and localized phonon modes has succeeded in a significant reduction of κ_l [7–11], sometimes to as low as the amorphous limit [12]. The general

consensus is that further improvement in ZT must come from the enhancement of the PF.

It is well known that sharply varying electronic density of states (DOS) near the Fermi level greatly benefits S and the PF [13,14]. The underlying mechanism is best illustrated by the well-known Mott formula [15], which for metals and heavily doped semiconductors simplifies to

$$S = -\frac{\pi^2 k_B^2 T}{3e} \frac{d \ln \sigma(E)}{dE}$$
$$= -\frac{\pi^2 k_B^2 T}{3e} \left[\frac{N'(E)}{N(E)} + \frac{\langle v^2(E) \rangle'}{\langle v^2(E) \rangle} + \frac{\tau'(E)}{\tau(E)} \right], \quad (1)$$

with the transport distribution function $\sigma(E) = e\tau(E)N(E)\langle v^2(E) \rangle$, where $N(E)$, $\tau(E)$, and $\langle v^2(E) \rangle$ are energy-dependent DOS, carrier lifetime, and mean of the squared group velocity, respectively. Clearly, large $N'(E)$ leads to high S. Ideas have been proposed to take advantage of this effect, such as designing for quantum confinement [16], introducing resonant impurity levels ("virtual bound states") [14,17], aligning light and heavy band pockets, and increasing valley degeneracy [18,19]. These methods, however, are limited to semiconductors, which have inherent band gaps that effectively separate the contributions of holes from those of electrons. Intermetallics naturally lack such gaps, allowing mutually excited electrons and holes

* yimaverickxia@gmail.com
† vidvuds.ozolins@yale.edu

to negate each others' contributions, leading to negligible S. Yet, since high electrical conductivity is usually guaranteed for intermetallics, even a modest improvement in S could lead to a very high PF. The question is how such an improvement can be made in spite of the unfavorable band structures.

We observe from Eq. (1) that while (i) the first two terms in the square brackets are fully determined by the static electronic band structure, (ii) the remaining term $\tau'(E)/\tau(E)$ is governed by dynamical processes, namely, carrier scattering mechanisms such as electron-phonon interaction (EPI), ionized impurity, and defect scattering. Then another way to increase S is for $\tau'(E)/\tau(E)$ to be large via the preferential scattering of low-energy electrons, a phenomenon commonly known as electron energy filtering [14,20]. To engineer strongly energy-dependent scattering, experimental studies have used "counterdoping" or potential energy barriers in two-dimensional (2D) structures [21,22], but these have only led to limited success. A question remains whether an intrinsic scattering process, such as EPI, can lead to strong enough energy filtering such that the $\tau'(E)/\tau(E)$ term dominates Eq. (1). Recently, it has been proposed by Xu *et al.* [23] that sizable S associated with boundary states in topological insulators is theoretically achievable, which arises from the strong energy dependence of the lifetime caused by edge-bulk interactions [23]. However, such effects have hardly been investigated and reported in conventional bulk thermoelectrics.

In this work, we report that the $B20$-type intermetallic CoSi exhibits strong EPI near the Fermi level that scatters low-energy electrons, thereby attaining large negative S and high PF. Though experimental studies have measured these previously [24–27], the underlying mechanism has not yet been well understood. Through state-of-the-art first-principles calculations, we attribute the strong EPI to the presence of a heavy band crossing the linear, massless (Dirac-like) bands just above the Fermi level, offering a scattering path for low-energy electrons. The band also bends below the Fermi level rather than above, providing a large phase space for hole scattering by phonons across a wide energy range but allowing electrons to maintain generally high lifetimes. Combined with large Fermi velocities of the massless bands, a remarkable power factor higher than 80 μW cm^{-1} K^{-2} is predicted at temperatures higher than 300 K. Our study constitutes a proof of concept that the coexistence of massless and heavy bands can lead to very high PFs in intermetallics.

II. THEORY AND COMPUTATIONAL DETAILS

Electron transport coefficients are calculated using the semiclassical Boltzmann transport equation (BTE) under relaxation time approximation (RTA) [28–30]. The key quantity required to compute the Seebeck coefficient S

and electrical conductivity σ is the transport distribution function $\sigma(E)$:

$$\sigma(E) = \frac{1}{N} \sum_{i,\mathbf{k}} e^2 \tau_{i,\mathbf{k}} \mathbf{v}_{i,\mathbf{k}} \otimes \mathbf{v}_{i,\mathbf{k}} \delta\left(E - E_{i,\mathbf{k}}\right), \quad (2)$$

where N, e, $\tau_{i,\mathbf{k}}$, $E_{i,\mathbf{k}}$, and $v_{i,\mathbf{k}}$ are the number of $\mathbf{k}$-points sampled, absolute charge of an electron, lifetime, energy, and group velocity for an electronic state with band and wave vector indexed by i and $\mathbf{k}$, respectively. The temperature T and chemical potential μ dependent S and σ at a given temperature T and chemical potential μ are

$$S(T,\mu) = -\frac{1}{eT} \frac{\int \sigma(E)(E-\mu)\left[\frac{-\partial f(T,E)}{\partial E}\right] dE}{\int \sigma(E)\left[\frac{-\partial f(T,E)}{\partial E}\right] dE}, \quad (3)$$

and

$$\sigma(T,\mu) = \frac{1}{\Omega} \int \sigma(E) \left[-\frac{\partial f(T,E)}{\partial E}\right] dE, \quad (4)$$

where Ω is the volume of a unit cell and $f(T,E)$ is the Fermi-Dirac distribution. Since CoSi is metallic, carriers are expected to be dominantly scattered via interactions with phonons at finite temperature. Therefore, $\tau_{i,\mathbf{k}}$ can be estimated using the imaginary part of electron self-energy from the first-order electron-phonon diagrams [31,32],

$$\begin{aligned}
\frac{1}{\tau_{i,\mathbf{k}}} = \frac{2\pi}{\hbar} \sum_{j,\nu} \int_{BZ} \frac{d\mathbf{q}}{\Omega_{BZ}} \left|g_{ji,\nu}(\mathbf{k},\mathbf{q})\right|^2 &\left(1 - \frac{\mathbf{v}_{\mathbf{k}} \cdot \mathbf{v}_{\mathbf{k}+\mathbf{q}}}{|\mathbf{v}_{\mathbf{k}}| \, |\mathbf{v}_{\mathbf{k}+\mathbf{q}}|}\right) \\
&\times [\left(n_{\nu,\mathbf{q}} + f_{j,\mathbf{k}+\mathbf{q}}\right) \delta\left(E_{i,\mathbf{k}} + \omega_{\nu,\mathbf{q}} - E_{j,\mathbf{k}+\mathbf{q}}\right) \\
&+ \left(1 + n_{\nu,\mathbf{q}} - f_{j,\mathbf{k}+\mathbf{q}}\right) \delta\left(E_{i,\mathbf{k}} - \omega_{\nu,\mathbf{q}} - E_{j,\mathbf{k}+\mathbf{q}}\right)],
\end{aligned} \quad (5)$$

where ν, $\mathbf{q}$, n, and ω are the phonon mode index, wave vector, population, and frequency, respectively. The velocity factor $\left[1 - (\mathbf{v}_{\mathbf{k}} \cdot \mathbf{v}_{\mathbf{k}+\mathbf{q}})/(|\mathbf{v}_{\mathbf{k}}| \, |\mathbf{v}_{\mathbf{k}+\mathbf{q}}|)\right]$ defines the momentum relaxation time in the BTE [31] and $g_{ji,\nu}(\mathbf{k},\mathbf{q})$ is an EPI matrix element.

We use QUANTUM ESPRESSO [33,34] to perform electronic structure calculations based on density function theory [35]. Troullier-Martins norm-conserving pseudopotentials [36] using the Perdew-Burke-Ernzerhof (PBE) [37] exchange-correlation (xc) functional [38] within the generalized gradient approximation (GGA) [39] are adopted. A kinetic energy cutoff of 75 Ry with a Methfessel-Paxton smearing [40] width of 0.015 Ry and Monkhorst-Pack grids of $8 \times 8 \times 8$ for $\mathbf{k}$-point sampling are used to ensure the convergence of total energy in self-consistent calculations. The lattice constant of the fully relaxed structure is 4.465 Å, which is in good agreement with the experimentally measured value of 4.450 Å

[41], despite slight overestimation of about 0.3%, which is typical within GGA. The band structure accounting for spin-orbit coupling is calculated using the fully relativistic pseudopotentials constructed using the ONCVPSP package [42].

The relaxation times limited by EPI are computed using the EPW package [32,43,44], which utilizes maximally localized Wannier functions (MLWFs) for efficient interpolation of EPI matrix elements onto a fine **k**-point mesh [32,45–49]. This interpolation scheme yields an accurate EPI matrix element at arbitrary sets of electron and phonon wave vectors at a much lower computational cost compared to direct linear response calculations, thus allowing dense sampling in both electron and phonon momentum space and ensuring good convergence of electron self-energy. Afterward, the momentum- and band-resolved relaxation time, i.e., $\tau_{i,\mathbf{k}}$, is used in BOLTZTRAP [29] to compute S and σ using densely sampled **k**-point and tetrahedron smearing method [50]. Hereinafter, we refer to the results obtained from this computational scheme as RTA. For a detailed description of the theory and further technical details, refer to the Supplemental Material [51].

To further elucidate the impact of the energy dependence of $\tau(E)$ on S, we also perform calculations under two other frequently used approximations, namely, (i) the constant relaxation time approximation (CRTA), where a single effective relaxation time is used in Eq. (2), and (ii) the DOS^{-1} approximation, which assumes that the relaxation time is only energy dependent and scales inversely to DOS. The DOS^{-1} approximation is generally superior to CRTA since it at least approximates the EPI phase space in evaluating $\tau(E)$, and it has been used by Xu *et al.* to successfully explain the nontrivial origin of positive S observed in lithium [52].

III. RESULTS AND DISCUSSIONS

A. Crystal and electronic structures

The $B20$-type CoSi belongs to space group $P2_13$, bearing a simple cubic structure with 4 Co and 4 Si atoms in a primitive cell, as shown in Fig. 1(a). The corresponding Brillouin zone is displayed in Fig. 1(b). We plot the band structure projected onto s, p, e_g, and t_{2g} states in Fig. 1(c). Near the Fermi level (± 1.5 eV), the bands are mainly composed of Co 3d states. Away from the Γ point, the band character shifts from e_g to t_{2g} states. The point of interest is that massless bands and a heavy band appear at and around the Γ point near the Fermi level, giving rise to a quadratic increase in DOS followed by a sharp step [see Fig. 1(d)]. Spin-orbit coupling is found to split the energies of the linear bands slightly, but largely preserve the Dirac-like and flat bands (see Fig. S1 in the Supplemental Material [51]). We did not include spin-orbit coupling in evaluating EPI due to the formidable computational cost and the minor effect on the band structure. It is worth noting, however,
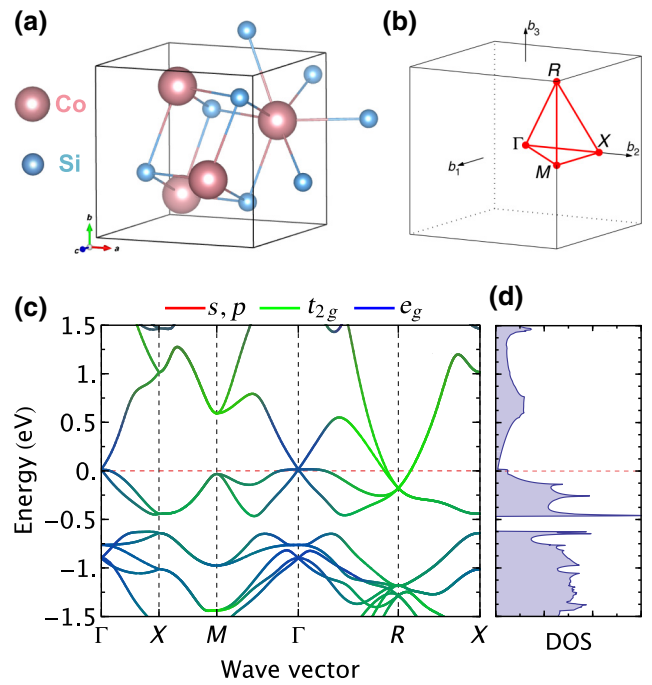

FIG. 1.   (a) Crystal structure, (b) Brillouin zone with high symmetry points, (c) electronic band structure, and (d) density of states (DOS) of $B20$-type CoSi. The Co and Si atoms are colored in red and blue, respectively. The band structure is color coded according to different orbitals shown in the legend, namely, s, p, e_g, and t_{2g} states.

that the presence of SOC could induce nontrivial topology of the electronic structure in $B20$-type CoSi, which has been recently reported by Tang *et al.* [53].

B. Seebeck coefficient, resistivity, and power factor

The calculated S under the CRTA, RTA, and DOS^{-1} approximation compared with experimental measurements is shown in Fig. 2(a). We see that the CRTA yields a small positive S and it changes sign to negative near 500 K. The positive S seems intuitively consistent with the larger DOS below the Fermi level than above. In contrast, all experimental measurements display negative S from modest 20 μV/K at 100 K to much larger 80 μV/K at 300 K and above. We find that the RTA results, which fully account for the momentum- and energy-resolved EPI, agree excellently with experiments and reproduce the observed temperature dependence of S. The DOS^{-1} approximation, which only accounts for the EPI phase space, is a significant improvement upon the CRTA and leads to S comparable with that obtained by the RTA, save for the overestimation of S at low temperatures (approximately 100 K).

To further verify the RTA results, we compare the predicted and experimentally measured hole-doping-induced sign change of S as a function of the Al substitution ratio
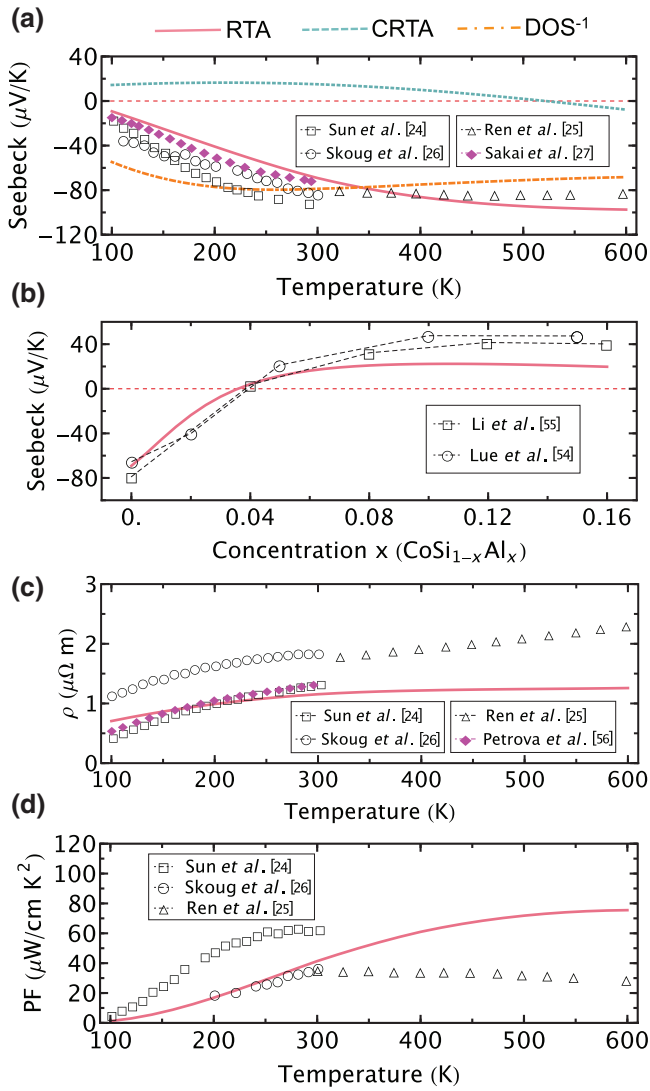
FIG. 2. (a) Calculated temperature-dependent Seebeck coefficient of pristine CoSi under RTA (red solid lines), CRTA (blue dashed lines), and DOS^{-1} approximation (orange dashed-dotted lines) in comparison with experimental measurements [24–27]. (b) Calculated Seebeck coefficient of $CoSi_{1-x}Al_x$ at various fractions of Al substitution on a Si site at 300 K compared with experiments [54,55]. The black dashed lines are given as guides to the eye. (c) Calculated temperature-dependent electrical resistivity of pristine CoSi in comparison with experiments [24–26,56]. (d) Calculated temperature-dependent power factor of pristine CoSi compared with experimental measurements [24–26]. In (a) and (c), experimental measurements performed on single crystals are denoted by magenta solid diamonds.

on the Si site [see Fig. 2(b)]. We find that 4% Al substitution is the critical point that induces a sign change of S from negative to positive, again agreeing well with experiments [54,55]. At a high Al concentration ($>10\%$), the calculated S is about one half of the experimental values [54,55]. We ascribe this discrepancy mainly to the possible

distortions in the electronic structure due to heavy doping. Figure 2(c) compares the calculated and experimental electrical resistivity. Clearly our calculations agree better with measurements performed on single crystals [56], while polycrystalline samples exhibit higher resistivity due to grain boundaries [25,26]. Experimentally measured values of the PF vary widely, as shown in Fig. 2(d), but our calculations agree reasonably well with Ref. [26], showing that a maximum PF of about 80 μW cm^{-1} K^{-2} for pristine CoSi is obtainable at 600 K.

Having confirmed the validity of RTA, we proceed to clarify the origin of the large negative S. A previous theoretical study on the B20-type CoGe with similar electronic structure has concluded that the large negative S originates from the asymmetric band structure about the Fermi level [57]. However, without considering energy-dependent carrier lifetimes, temperature and doping dependencies deviate considerably from experimental results. A key quantity that determines S and σ [see Eqs. (3) and (4)] is the transport distribution function $\sigma(E)$. For S to be large, asymmetric $\sigma(E)$ is required, while for σ to be large, an overall high $\sigma(E)$ in the energy window spanned by the Fermi-Dirac distribution near the Fermi level is all that is needed. Figure 3(a) displays the calculated $\sigma(E)$ under the CRTA, RTA, and DOS^{-1} approximation at 300 K. It is evident that $\sigma(E)$ under the CRTA deviates significantly from those under the other two approximations. The latter two are strongly asymmetric about the Fermi level, while the former fails to capture this. Since the CRTA already takes into account both the $N(E)$ and $\langle v^2(E) \rangle$ terms in Eq. (1), it is conclusive that the strong energy dependence of $\tau(E)$ plays the central role in determining the overall transport behavior, as evidenced by comparing the RTA and CRTA results in Fig. 2(a). Figure 3(b) clearly shows the otherwise long electron lifetimes dropping quickly near the Fermi level. An analysis of the band structure elucidates that it is the abrupt change of DOS slightly above the Fermi level, which arises from the flat band, that leads to preferential scattering of low-energy electrons in the massless bands (energy filtering), thus creating a large gradient in $\tau(E)$. In addition, the hole lifetimes are short due to the much larger hole DOS near the Fermi level, allowing electrons to dominate transport. The DOS^{-1} approximation, despite its simplicity, qualitatively reflects the energy dependence of $\tau(E)$ and thereby the asymmetric behavior of $\sigma(E)$. This suggests that EPI phase space probably dominates over the specific strength of EPI matrix elements in determining the energy dependence of carrier lifetimes.

Because of the abrupt change of DOS (see Fig. S5 in the Supplemental Material [51]), we also find it crucial to use an accurately determined Fermi level at each temperature by accounting for the Fermi-Dirac distribution. Our calculated resistivity exhibits unusual temperature dependence; that is, it is nearly independent of temperature above 300 K [see Fig. 2(c)]. This contrasts the typical
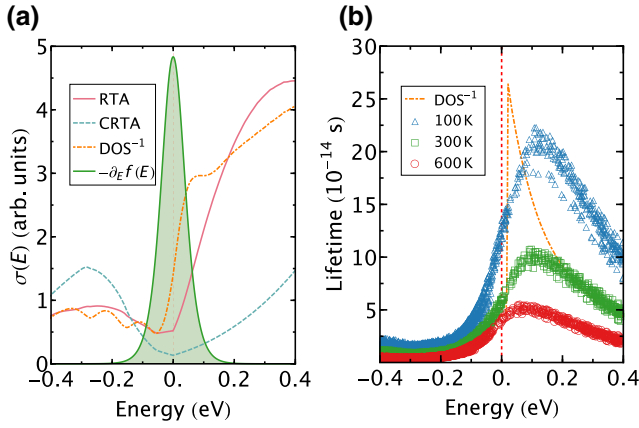
FIG. 3. (a) Calculated transport distribution function $\sigma(E)$ under RTA (red solid lines), CRTA (blue dashed lines), and DOS^{-1} approximation (orange dashed-dotted lines) at 300 K. The light green area indicates the energy window restricted by the energy derivative of the Fermi-Dirac distribution. (b) Calculated energy-dependent carrier lifetimes at 100 K (blue triangles), 300 K (green squares), and 600 K (red circles) compared with a scaled DOS^{-1} approximation (orange dashed-dotted lines).

behavior of increasing resistivity with temperature due to intensifying EPI. Unsurprisingly, a reduction in lifetime with increased temperature is observed, as shown in Fig. 3(b). However, the Fermi level also shifts toward higher energy due to the broadening Fermi-Dirac distribution (see Fig. S5 in the Supplemental Material [51]). Concomitantly, the mean Fermi velocity increases as more electrons are excited into the Dirac bands, partially counteracting the effect of lifetime reduction. The net effect is a nearly temperature-independent electrical resistivity from 300 to 600 K. To further confirm our theoretical prediction, experimental measurements on high-quality single crystal CoSi at temperatures above 300 K are suggested.

C. Effects of temperature and doping

Finally, we map out the temperature and doping dependence of S and PF in Fig. 4. While S can still be optimized with slight electron doping at low temperatures, it is already nearly optimal in pristine CoSi at high temperatures. Increasing the temperature tends to enhance S for samples with both electron and hole doping. As we observed previously, hole doping tends to shift S to positive value as it reduces the asymmetric behavior of $\sigma(E)$ near the Fermi level. Concerning the PF, a value larger than 60 μW cm^{-1} K^{-2} can be achieved at temperatures as low as 200 K with slight electron doping (approximately 0.01/f.u.). Increasing the temperature above 300 K can further lead to an optimal PF of 80 μW cm^{-1} K^{-2} or higher, while hole doping tends to rapidly decrease the PF. Heavy hole doping, which leads to small positive S and high electrical resistivity, significantly reduces the PF. Our
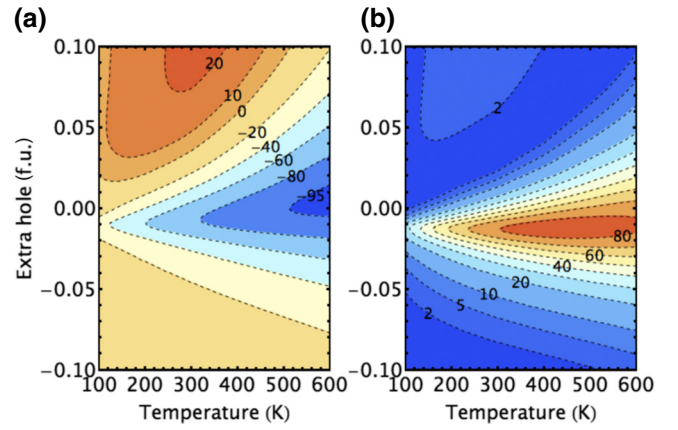

FIG. 4. Contour plot of calculated (a) Seebeck coefficient in μV K^{-1} and (b) power factor in μW cm^{-1} K^{-2} as a function of temperature and extra hole per formula unit (CoSi$_{1-x}$Al$_x$).

study highlights the possibility to achieve large S and PF in metallic compounds with the simultaneous occurrence of Dirac-like bands for mobile transport and a flat band as an energy filter near the Fermi level.

To further illustrate the high PF of CoSi, in Fig. 5 we compare the theoretically maximized temperature-dependent PF of CoSi to the PFs of two classical thermoelectric materials, Bi$_2$Te$_3$ [58] and PbTe [59], and a recently identified high-performance thermoelectric with record ZT, SnSe [60], as well as two other compounds FeNbSb [61] and YbAl$_3$ [62], which currently hold the record PFs for bulk semiconductors and intermetallics, respectively. Compared to semiconducting Bi$_2$Te$_3$, PbTe, and SnSe, CoSi has a much higher PF across the whole temperature range from 300 to 600 K, mostly because of the low electrical resistivity in spite of the relatively small Seebeck coefficient. Our theoretically optimized PF of CoSi is comparable with that of FeNbSb, which has recently been reported to possess a record output power density of about 22 W cm^{-2} [61]. The intermetallic YbAl$_3$ exhibits an ultrahigh PF at 300 K, where the anomalous Seebeck coefficients arise from Kondo resonance [63] and virtual bound states [64]. However, the PF of YbAl$_3$ decreases sharply with increased temperature, making it significantly smaller than that of CoSi at 600 K. Considering the fact that the high PF of CoSi remains almost constant in the entire temperature range, CoSi may be used as a Peltier cooler with a potential application for electronic cooling, where both large PF and thermal conductivity are desired [65].

D. General remarks

Instructive comparisons can be drawn between CoSi and some relevant cases. Recently, it has been brought to light that, for Dirac-like bands, the electron mean free path (MFP) monotonically decreases with energy, leading
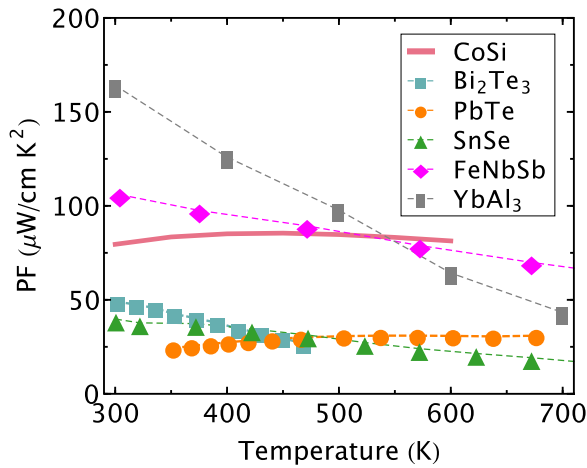
FIG. 5.   Theoretically optimized temperature-dependent power factor of CoSi compared to several state-of-the-art thermoelectric materials with experimentally achieved high power factors, namely, semiconducting Bi_2Te_3 [58], PbTe [59], SnSe [60], FeNbSb [61], and intermetallic $YbAl_3$ [62].

to the concept of filtering electrons by long MFP, which automatically filters out low-energy electrons [66]. However, this has required nanostructuring of 10-nm grains in SnTe. Energy filtering by inherent EPI as in CoSi does not require such an expensive process, which is another advantage. Nonetheless, some degree of nanostructuring of CoSi would still benefit ZT by reducing lattice thermal conductivity, since its ZT is severely handicapped by the large bulk κ_l that exceeds 10 W/mK at 300 K [67]. Furthermore, the coexistence of massless and heavy bands in CoSi is reminiscent of flat-and-dispersive,"low-dimensional" band structures, which has been a concept for high-PF semiconductor thermoelectrics [68,69]. However, recent work suggests that such a band structure is not as beneficial as purely dispersive bands for semiconductors [70]. This owes partly to the fact that bipolar transport is not an issue for doped semiconductors and S is naturally large. Therefore, while the flat band may contribute DOS and function as a low-energy electron filter, both to the potential extra benefit of S, it is eclipsed by the general surge in scattering rates (reduction of lifetimes), a severe detriment to mobility. Ultimately, the presence of the flat band is likely to cause more overall harm than good for the PF in semiconductors. This situation directly contrasts with the case of intermetallics, for which the categorical need to sustain non-negligible S outweighs the loss of lifetimes due to scattering, especially since high conductivity is ensured.

IV. CONCLUSIONS

In summary, we use a first-principles approach with explicit calculations of electron-phonon interaction to investigate the thermoelectric properties of the $B20$-type intermetallic CoSi, with the main goal of identifying

the origin of the large negative Seebeck coefficient. We find that the large Seebeck coefficient arises from the heavily energy-dependent carrier lifetimes due to strong electron-phonon interaction. The strong electron-phonon interaction is invited by a heavy band that crosses linear bands near the Fermi level, providing a large phase space for electron-phonon scattering. Combined with the large Fermi velocity of the massless bands, remarkable power factors of 80 μW cm^{-1} K^{-2} or higher are predicted over a wide temperature range from 300 to 600 K with slight adjustments in the Fermi level. Our study shows that efficient energy filtering by electron-phonon interactions can generate a large Seebeck coefficient and high power factor in metallic compounds. We hope that these results will serve as a motivation for renewed efforts in identifying high-performance thermoelectrics among intermetallic compounds.

[1] J. Sootsman, D. Chung, and M. Kanatzidis, New and old concepts in thermoelectric materials, Angew. Chem. Int. Ed. **48**, 8616 (2009).

[2] G. J. Snyder and E. S. Toberer, Complex thermoelectric materials, Nat. Mater. **7**, 105 (2008).

[3] X. Zhang and L.-D. Zhao, Thermoelectric materials: Energy conversion between heat and electricity, J. Materiomics **1**, 92 (2015).

[4] X. Shi, L. Chen, and C. Uher, Recent advances in high-performance bulk thermoelectric materials, Int. Mater. Rev. **61**, 379 (2016).

[5] X. Zhou, Y. Yan, X. Lu, H. Zhu, X. Han, G. Chen, and Z. Ren, Routes for high-performance thermoelectric materials, Mater. Today **21**, 974 (2018).

[6] D. Rowe, *CRC Handbook of Thermoelectrics* (CRC Press, Florida, 1995).

[7] K. Biswas, J. He, I. D. Blum, C.-I. Wu, T. P. Hogan, D. N. Seidman, V. P. Dravid, and M. G. Kanatzidis, High-performance bulk thermoelectrics with all-scale hierarchical architectures, Nature **489**, 414 (2012).

[8] E. J. Skoug and D. T. Morelli, Role of Lone-Pair Electrons in Producing Minimum Thermal Conductivity in Nitrogen-Group Chalcogenide Compounds, Phys. Rev. Lett. **107,** 235901 (2011).

[9] X. Lu, D. T. Morelli, Y. Xia, F. Zhou, V. Ozoliņš, H. Chi, X. Zhou, and C. Uher, High performance thermoelectricity in earth-abundant compounds based on natural mineral tetrahedrites, Adv. Energy Mater. **3,** 342 (2013).

[10] L.-D. Zhao, S.-H. Lo, Y. Zhang, H. Sun, G. Tan, C. Uher, C. Wolverton, V. P. Dravid, and M. G. Kanatzidis, Ultralow thermal conductivity and high thermoelectric figure of merit in SnSe crystals, Nature **508,** 373 (2014).

[11] T. Takabatake, K. Suekuni, T. Nakayama, and E. Kaneshita, Phonon-glass electron-crystal thermoelectric clathrates: Experimentsand theory, Rev. Mod. Phys. **86,** 669 (2014).

[12] G. A. Slack, *CRC Handbook of Thermoelectrics* (CRC Press, Boca Raton, FL, 1995), p. 407.

[13] G. D. Mahan and J. O. Sofo, The best thermoelectric, Proc. Natl. Acad. Sci. U.S.A **93,** 7436 (1996).

[14] J. P. Heremans, B. Wiendlocha, and A. M. Chamoire, Resonant levels in bulk thermoelectric semiconductors, Energy Environ. Sci. **5,** 5510 (2012).

[15] N. Mott and E. Davis, *Electronic Processes in Non-crystalline Materials*, International Series of Monographs on Physics (Clarendon Press, 1971).

[16] L. D. Hicks and M. S. Dresselhaus, Effect of quantum-well structures on the thermoelectric figure of merit, Phys. Rev. B **47,** 12727 (1993).

[17] J. P. Heremans, V. Jovovic, E. S. Toberer, A. Saramat, K. Kurosaki, A. Charoenphakdee, S. Yamanaka, and G. J. Snyder, Enhancement of thermoelectric efficiency in PbTe by distortion of the electronic density of states, Science **321,** 554 (2008).

[18] Y. Pei, X. Shi, A. LaLonde, H. Wang, L. Chen, and G. J. Snyder, Convergence of electronic bands for high performance bulk thermoelectrics, Nature **473,** 66 (2011).

[19] Y. Pei, H. Wang, and G. J. Snyder, Band engineering of thermoelectric materials, Adv. Mater. **24,** 6125 (2012).

[20] J.-H. Bahk, Z. Bian, and A. Shakouri, Electron energy filtering by a nonplanar potential to enhance the thermoelectric power factor in bulk materials, Phys. Rev. B **87,** 075204 (2013).

[21] J.-P. Issi, J.-P. Michenaud, and J. Heremans, Electron scattering in compensated bismuth, Phys. Rev. B **14,** 5156 (1976).

[22] T. E. Humphrey and H. Linke, Reversible Thermoelectric Nanomaterials, Phys. Rev. Lett. **94,** 096601 (2005).

[23] Y. Xu, Z. Gan, and S.-C. Zhang, Enhanced Thermoelectric Performance and Anomalous Seebeck Effects in Topological Insulators, Phys. Rev. Lett. **112,** 226801 (2014).

[24] H. Sun, X. Lu, and D. T. Morelli, Effects of Ni, Pd, and Pt substitutions on thermoelectric properties of CoSi alloys, J. Electron. Mater. **42,** 1352 (2013).

[25] W. Ren, C. Li, L. Zhang, K. Ito, and J. Wu, Effects of Ge and B substitution on thermoelectric properties of CoSi, J. Alloy. Compd. **392,** 50 (2005).

[26] E. Skoug, C. Zhou, Y. Pei, and D. T. Morelli, High thermoelectric power factor in alloys based on CoSi, Appl. Phys. Lett. **94,** 022115 (2009).

[27] A. Sakai, S. Yotsuhashi, H. Adachi, F. Ishii, Y. Onose, Y. Tomioka, N. Nagaosa, and Y. Tokura, in *Thermoelectrics, 2007. 26th International Conference on ICT 2007* (2007), p. 256.

[28] M. Cutler and N. F. Mott, Observation of Anderson localization in an electron gas, Phys. Rev. **181,** 1336 (1969).

[29] G. K. Madsen and D. J. Singh, BoltzTraP. A code for calculating band-structure dependent quantities, Comput. Phys. Commun. **175,** 67 (2006).

[30] J. Ziman, *Electrons and Phonons: The Theory of Transport Phenomenain Solids*, International Series of Monographs on Physics (OUP Oxford, 1960).

[31] G. Mahan, *Many-Particle Physics, Physics of Solids and Liquids* (Springer, New York, 2000).

[32] F. Giustino, M. L. Cohen, and S. G. Louie, Electron-phonon interaction using Wannier functions, Phys. Rev. B **76,** 165108 (2007).

[33] P. Giannozzi *et al.*, QUANTUM ESPRESSO: A modular and open-source software project for quantum simulations of materials, J. Phys.: Condens. Matter **21,** 395502 (2009).

[34] P. Giannozzi *et al.*, Advanced capabilities for materials modelling with Q uantum ESPRESSO, J. Phys.: Condens. Matter **29,** 465901 (2017).

[35] P. Hohenberg and W. Kohn, Inhomogeneous electron gas, Phys. Rev. **136,** B864 (1964).

[36] N. Troullier and J. L. Martins, Efficient pseudopotentials for plane-wave calculations, Phys. Rev. B **43,** 1993 (1991).

[37] J. P. Perdew, K. Burke, and M. Ernzerhof, Generalized Gradient Approximation Made Simple, Phys. Rev. Lett. **77,** 3865 (1996).

[38] W. Kohn and L. J. Sham, Self-consistent equations including exchange and correlation effects, Phys. Rev. **140,** A1133 (1965).

[39] J. P. Perdew, K. Burke, and Y. Wang, Generalized gradient approximation for the exchange-correlation hole of a many-electron system, Phys. Rev. B **54,** 16533 (1996).

[40] M. Methfessel and A. T. Paxton, High-precision sampling for Brillouin-zone integration in metals, Phys. Rev. B **40,** 3616 (1989).

[41] P. Demchenko, J. Konczyk, O. Bodak, R. Matvijishyn, L. Muratova, and B. Marciniak, Single crystal investigation of the new phase $Er_{0.85}Co_{4.31}Si$ and of CoSi, Chem. Met. Alloys **1,** 50 (2008).

[42] D. R. Hamann, Optimized norm-conserving Vanderbilt pseudopotentials, Phys. Rev. B **88,** 085117 (2013).

[43] S. Poncé, E. Margine, C. Verdi, and F. Giustino, EPW: Electron–phonon coupling, transport and superconducting properties using maximally localized Wannier functions, Comput. Phys. Commun. **209,** 116 (2016).

[44] J. Noffsinger, F. Giustino, B. D. Malone, C.-H. Park, S. G. Louie, and M. L. Cohen, EPW: A program for calculating the electron–phonon coupling using maximally localized Wannier functions, Comput. Phys. Commun. **181,** 2140 (2010).

[45] N. Marzari and D. Vanderbilt, Maximally localized generalized Wannier functions for composite energy bands, Phys. Rev. B **56,** 12847 (1997).

[46] I. Souza, N. Marzari, and D. Vanderbilt, Maximally localized Wannier functions for entangled energy bands, Phys. Rev. B **65,** 035109 (2001).

[47] N. Marzari, A. A. Mostofi, J. R. Yates, I. Souza, and D. Vanderbilt, Maximally localized Wannier functions: Theory and applications, Rev. Mod. Phys. **84,** 1419 (2012).

[48] A. A. Mostofi, J. R. Yates, Y.-S. Lee, I. Souza, D. Vanderbilt, and N. Marzari, wannier90: A tool for obtaining maximally-localised Wannier functions, Comput. Phys. Commun. **178,** 685 (2008).

[49] F. Giustino, Electron-phonon interactions from first principles, Rev. Mod. Phys. **89,** 015003 (2017).

[50] P. E. Blöchl, O. Jepsen, and O. K. Andersen, Improved tetrahedron method for Brillouin-zone integrations, Phys. Rev. B **49,** 16223 (1994).

[51] See the Supplemental Material at http://link.aps.org/supple mental/10.1103/PhysRevApplied.11.024017 for a detailed description of the computational methods used in this work. Furthermore, detailed descriptions of the computational parameters, electron-phonon Wannier interpolation, impact of spin-orbit coupling on band structure, and temperature-dependent Fermi level are presented.

[52] B. Xu and M. J. Verstraete, First Principles Explanation of the Positive Seebeck Coefficient of Lithium, Phys. Rev. Lett. **112,** 196603 (2014).

[53] P. Tang, Q. Zhou, and S.-C. Zhang, Multiple Types of Topological Fermions in Transition Metal Silicides, Phys. Rev. Lett. **119,** 206402 (2017).

[54] C. S. Lue, Y.-K. Kuo, C. L. Huang, and W. J. Lai, Hole-doping effect on the thermoelectric properties and electronic structure of CoSi, Phys. Rev. B **69,** 125111 (2004).

[55] C. C. Li, W. L. Ren, L. T. Zhang, K. Ito, and J. S. Wu, Effects of Al doping on the thermoelectric performance of CoSi single crystal, J. Appl. Phys. **98,** 063706 (2005).

[56] A. E. Petrova, V. N. Krasnorussky, A. A. Shikov, W. M. Yuhasz, T. A. Lograsso, J. C. Lashley, and S. M. Stishov, Elastic, thermodynamic, and electronic properties of MnSi, FeSi, and CoSi, Phys. Rev. B **82,** 155124 (2010).

[57] N. Kanazawa, Y. Onose, Y. Shiomi, S. Ishiwata, and Y. Tokura, Band-filling dependence of thermoelectric properties in B20-type CoGe, Appl. Phys. Lett. **100,** 093902 (2012).

[58] D. Lo, R.-R. Sun, and X.-D. Qin, Improving thermoelectric properties of p-type Bi_2Te_3-based alloys by spark plasma sintering, Pro. Nat. Sci.-Mater. **21,** 336 (2011).

[59] J. Sootsman, H. Kong, C. Uher, J. D'Angelo, C.-I. Wu, T. Hogan, T. Caillat, and M. Kanatzidis, Large enhancements in the thermoelectric power factor of bulk pbte at high temperature by synergistic nanostructuring, Angew. Chem. Int. Ed. **47,** 8618 (2008).

[60] L.-D. Zhao, G. Tan, S. Hao, J. He, Y. Pei, H. Chi, H. Wang, S. Gong, H. Xu, V. P. Dravid, C. Uher, G. J. Snyder, C. Wolverton, and M. G. Kanatzidis, Ultrahigh power factor and thermoelectric performance in hole-doped single-crystal SnSe, Science **351,** 141 (2016).

[61] R. He, D. Kraemer, J. Mao, L. Zeng, Q. Jie, Y. Lan, C. Li, J. Shuai, H. S. Kim, Y. Liu, D. Broido, C.-W. Chu, G. Chen, and Z. Ren, Achieving high power factor and output power density in p-type half-Heuslers $Nb_{1-x}Ti_xFeSb$, Proc. Natl. Acad. Sci. U.S.A **113,** 13576 (2016).

[62] D. M. Rowe, V. L. Kuznetsov, L. A. Kuznetsova, and G. Min, Electrical and thermal transport properties of intermediate-valence $YbAl_3$, J. Phys. D: Appl. Phys. **35,** 2183 (2002).

[63] U. Walter, E. Holland-Moritz, and Z. Fisk, Kondo resonance in the neutron spectra of intermediate-valent $YbAl_3$, Phys. Rev. B **43,** 320 (1991).

[64] C. L. Foiles, Thermoelectric power of dilute Cu-Ni alloys in a magnetic field, Phys. Rev. **169,** 471 (1968).

[65] M. Zebarjadi, Electronic cooling using thermoelectric devices, Appl. Phys. Lett. **106,** 203506 (2015).

[66] T.-H. Liu, J. Zhou, M. Li, Z. Ding, Q. Song, B. Liao, L. Fu, and G. Chen, Electron mean-free-path filtering in Dirac material for improved thermoelectric performance, Proc. Natl. Acad. Sci. U.S.A **115,** 879 (2018).

[67] H. Sun and D. T. Morelli, Thermoelectric properties of $Co_{1-x}Rh_xSi_{0.98}B_{0.02}$ alloys, J. Electron. Mater. **41,** 1125 (2012).

[68] D. Parker, X. Chen, and D. J. Singh, High Three-Dimensional Thermoelectric Performance from Low-Dimensional Bands, Phys. Rev. Lett. **119,** 146691 (2013).

[69] D. I. Bilc, G. Hautier, D. Waroquiers, G.-M. Rignanese, and P. Ghosez, Low-Dimensional Transport and Large Thermoelectric Power Factors in Bulk Semiconductors by Band Engineering of Highly Directional Electronic States, Phys. Rev. Lett. **114,** 136601 (2015).

[70] J. Park, Y. Xia, and V. Ozoliņš, High Thermoelectric Power Factor and Efficiency from a Highly Dispersive Band in Ba_2BiAu, Phys. Rev. Applied **11,** 014058 (2019).